AnnRG - An artificial neural network solute geothermometer

Lars H. Ystroem [*], Mark Vollmer, Thomas Kohl, Fabian Nitschke

Karlsruhe Institute of Technology (KIT), Institute of Applied Geoscience (AGW), Division of Geothermal Energy and Reservoir Technology, Campus South, Adenauerring 20b, 76131, Karlsruhe, Germany

ARTICLE INFO

ABSTRACT

Solute artificial neural network geothermometers offer the possibility to overcome the complexity given by the solute-mineral composition. Herein, we present a new concept, trained from high-quality hydrochemical data and verified by *in-situ* temperature measurements with a total of 208 data pairs of geochemical input parameters (Na$^+$, K$^+$, Ca^{2+}, Mg^{2+}, Cl$^-$, SiO$_2$, and pH) and reservoir temperature measurements being compiled. The data comprises nine geothermal sites with a broad variety of geochemical characteristics and enthalpies. Five sites with 163 samples (Upper Rhine Graben, Pannonian Basin, German Molasse Basin, Paris Basin, and Iceland) are used to develop the ANN geothermometer, while further four sites with 45 samples (Azores, El Tatio, Miavalles, and Rotorua) are used to encounter the established artificial neural network in practice to unknown data. The setup of the application, as well as the optimisation of the network architecture and its hyperparameters, are stepwise introduced. As a result, the solute ANN geothermometer, AnnRG (Artificial neural network Regression Geothermometer), provides precise reservoir temperature predictions (RMSE of 10.442 K) with a high prediction accuracy of $R^2 = 0.978$. In conclusion, the implementation and verification of the first adequate ANN geothermometer is an advancement in solute geothermometry. Our approach is also a basis for further broadening and refining applications in geochemistry.

1. Introduction

Geothermometry constitutes an important geochemical tool for reservoir temperature determination. The unperturbed reservoir temperature predictions are a key parameter for the exploration and development of geothermal resources in the subsurface (Arnórsson, 2000a). In solute geothermometry, the geochemical composition of the geothermal fluid reflects the temperature-dependent equilibrium state between reservoir and fluid (Ellis and Mahon, 1964). The saturation state of mineral phases as well as specific cation ratios are dependent on the thermal conditions at depth and therefore can be used to infer the reservoir temperature (Fournier and Truesdell, 1974). In the 1960s the first conventional solute geothermometer was presented, which empirically linked the silica concentration in hot springs to the associated quartz equilibrium temperature at depth (Fournier and Rowe 1966). Since then, continuously new geothermometers have been developed or improved. Most applications of solute geothermometers are based on SiO$_2$ concentration as well as the major cation ratios of Na/K, Na/K/Ca, and K^2/Mg (Fournier and Truesdell, 1973; Fournier and Potter, 1979, 1982; Giggenbach, 1988; Arnórsson, 2000b). Na$^+$, K$^+$, Ca^{2+}, and Mg^{2+}

are the major cations encountered in crustal rocks and geothermal water, whereas Cl$^-$ and SO$_4^{2-}$ are the major anions (Giggenbach, 1988). The monovalent cations, Na$^+$ and K$^+$, are mostly controlled by the ratio corresponding to the equilibrium state of albite and K-feldspar (Ellis and Mahon, 1964). In hydrothermal systems, the Ca^{2+} concentration is mostly given by the temperature and salinity-dependent solubility of calcite and calcium-aluminium-silicates (Ellis, 1963; Giggenbach, 1981). Likewise, Mg^{2+} is controlled by the solubility of K–Mg layer silicates, which is chlorite-dependent (Giggenbach, 1988). In geothermal fluids the silica concentration is driven by reservoir conditions regarding chalcedony or quartz equilibrium (Fournier and Rowe, 1966) with pH values in a broad range from acidic to alkaline conditions linked to the activity of hydrogen ions. Like the salinity, the pH value influences the ionic activity of the geothermal fluid (Debye and Hückel, 1923; Davies, 1938).

Due to the implementation of conventional geothermometers on regional geochemical data, the application is prone to variation in the chemical composition of geothermal fluid. This leads to high uncertainties regarding reservoir temperature predictions (Nitschke et al., 2017). Based on the evaluation of the saturation state of multiple

---

aforementioned mineral phases, Reed and Spycher (1984) introduced an alternative approach by computing saturation curves based on thermodynamic solubility data of a set of reservoir minerals against temperature. In contrast to conventional geothermometers based on element concentrations and ratios, the saturation indices of multiple mineral phases need to be calculated to predict the reservoir temperature. Thereby, the aqueous ions concentration of the geothermal fluid is compared to the equilibrium concentration of the temperature-dependent solubility of the mineral phases. The clustering of the mineral's equilibrium temperatures in the chemical system of fluid and reservoir rock are indicating the reservoir temperature. Reed and Spycher (1984) already revealed that the results are statistically more robust than conventional geothermometers, which have often been proven to be afflicted with larger uncertainties (Pang, 1988; Pang and Reed, 1998; Nitschke et al., 2017, 2018).

Nevertheless, the multicomponent geothermometer is still prone to secondary perturbations of the equilibrium of the geothermal fluid, such as mixing, boiling and dilution, precipitation and dissolution, or analytical errors (Pang, 1988; Pang and Reed, 1998). The different tools have been developed with integrated optimisation processes correcting the error of fluid perturbation: 1) WATCH (Bjarnason, 2010), using analyses of the sampled water, gas, condensate, and excess enthalpy to compute the reservoir composition of the fluid (the aqueous speciation, the pH and redox potential, and the partial pressure of gas phases) (Arnórsson et al., 1982). 2) RTEst (Palmer, 2014) using temperature, CO_2 fugacity, and a mixing fraction by minimising the saturation indices of a suggested mineral set (Palmer et al., 2014). 3) iGeoT automatically estimates input parameters, such as the factor of concentration/dilution, the steam weight fraction, as well as input concentrations of aqueous and gas species, using the iTOUGH2 numerical optimisation engine (Spycher and Finsterle, 2016). With PyGeoT, a pre- and post-processing script is developed for automated mineral assemblage selection for GeoT/iGeoT (Olguín-Martínez et al., 2022). 4) MulT_predict being firstly introduced with distinct numerical optimisation for aluminium concentration, pH value, and steam loss/dilution, as well as an individual high temperature (up to 350 °C) mineral assemblage for basalt settings (Ystroem et al., 2020). These optimisation processes were merged into an interdependent back-calculation of reservoir conditions (Ystroem et al., 2021). For worldwide applicability, a universally valid mineral assemblage for unknown reservoir composition, a procedure of outlier removal, and the limits of MulT_predict are developed (Ystroem et al., 2022), demonstrating the broad and accurate applicability of solute multicomponent geothermometers with integrated optimisation processes. However, the computational effort rises dramatically with the number of optimisation processes while the back-calculation of fluid perturbations requires necessary geochemical preknowledge.

This situation provides ideal starting conditions for the application of machine learning (ML) algorithms to support automated numerical optimisation programs. Compared to other natural sciences, ML is particularly rarely used in geochemical interpretation. This is largely due to the limited amount of data available, as geochemical analyses are usually difficult to obtain at great expense. At the same time, the heterogeneity of the subsurface and physical parameters limits the extrapolation of the collected data. Also, the application of ML techniques has been strongly increased in geosciences recently. This development is favoured by free software libraries such as *Scikit-learn* (Pedregosa et al., 2011) or *TensorFlow* (Abadi et al., 2015) enabling easy access to ML in various programming environments. Likewise, literature and documentation such as Goodfellow et al. (2016) educate the structure and functionality of deep learning algorithms. ML is also favoured by the steady increase in geoscientific, complex data to be statistically evaluated (Dramsch, 2020) and the increase in computational power (Reichstein et al., 2019). The present paper supports this development with respect to geochemical analyses, which have been studied far less than other geoscience data because of their general complexity.

Geochemical fluid analyses are inflicted by a complexity of

parameters that are mostly coupled with each other and the underlying thermodynamics. In the early 2000s, the first attempts have been made to use artificial neural networks (ANNs) for geochemical data analysis. In geothermometry, Ferhat Bayram (2001), Can (2002) as well as Díaz-González et al. (2008) used ML for data regression improving conventional Na/K geothermometer methods. In addition, the first gaseous ANN geothermometer was introduced by Pérez-Zárate et al. (2019), using CO_2, H_2S, CH_4, and H_2 concentration as input parameters. Haklidir and Haklidir (2020) developed the first deep neural network (DNN) solute geothermometer approach based on chemical multi-parameter analysis (pH, electrical conductivity, K^+, Na^+, Li^+, B_{total}, SiO_2, and Cl^-). Nevertheless, this study is based on a small dataset of 83 samples. To increase the training data size to 66 samples, Haklidir and Haklidir (2020) predicted the reservoir temperature of 47 thermal springs by applying the conventional solute geothermometer of Fournier (1977) in advance. Therefore, this DNN approach is also prone to error propagation, since more than 70% of the training data are already reservoir temperature predictions comprising the uncertainties of conventional geothermometers. These predictions are then used to develop a DNN for reservoir temperature prediction for the regional case. Based on the data of Haklidir and Haklidir (2020), Ibrahim et al. (2023) tested five ML algorithms for their temperature prediction performance and the shapley additive explanation (SHAP) (Lundberg and Lee, 2017) to determine the contribution of each input parameter to the ML models. In addition, Altay et al. (2022) also used the data of Haklidir and Haklidir (2020) and others to test multiple machine learning methods to predict reservoir temperatures in Anatolia. A grey wolf optimiser multi-layer perceptron (GWO-MLP) showed good results, which then was further improved (Altay and Altay, 2023).

This manuscript demonstrates the development of an adequate solute ANN geothermometer, called AnnRG, which is only trained using geochemical data and *in-situ* temperature measurements of geothermal sites. No reservoir temperatures have to be predicted in advance to increase the data size, leading to less error propagation. This new ML study focuses on complex and heterogeneous geochemical data comprising thermodynamic coupling of system parameters and element concentrations. In regard to the numerically optimised multicomponent geothermometers, strong benefits in computation time are expected. The motivation is to establish an easy-to-apply ANN solute geothermometer for accurate reservoir temperature prediction without the need for sophisticated geochemical preknowledge such as geochemical equilibrium processes or reservoir mineral assemblages.

2. Data & methods

2.1. Data acquisition

A key aspect of the development of AnnRG (Artificial neural network Regression Geothermometer) is the acquisition of a high-quality dataset consisting of the chemical analysis of fluid samples and their in-situ measured reservoir temperature. This combination including high data quality and large datasets is unfortunately rare and such data are difficult to obtain. In sum, nine geothermal sites with a broad variety of geochemical characteristics and enthalpies are evaluated (cf. Table 1). This data can be distinguished into five sites according to their origin (Upper Rhine Graben, Pannonian Basin, German Molasse Basin, Paris Basin, and Iceland), which are used for the development of AnnRG, and further four sites (Azores, El Tatio, Miavalles, and Rotorua) to encounter the ANN in practice to unknown data. The location of the geothermal field is plotted in Fig. 1.

Well data consisting of the chemical fluid composition and the reservoir temperature is a key factor for avoiding the effects of data perturbation. To develop the geothermometer, five well-studied geothermal fields have been identified from which such data is available. In the Upper Rhine Graben, the geothermal fluids of the rift basin represent a highly saline Na^+-Cl^- type (up to 200 g/l) (Pauwels et al.,

Table 1

Collection of geochemical fluid analyses and measured in-situ temperatures of five geothermal sites to merge a dataset as the basis of the ANN geothermometer. In addition, four geothermal sites are used to verify the developed ANN geothermometer (separated by a line). In addition, the available sample size, the lithology, and the temperature range per site are given.

Data	Sample size	Lithology	Temperature range	Reference
Upper Rhine Graben	40	Granite, Germanic Trias facies, Permian facies	41 °C–200 °C	Pauwels et al. (1993); Aquilina et al. (1997); Vaute et al. (1998); Sanjuan et al. (2001); Sanjuan et al. (2004); Sanjuan et al. (2006); Sanjuan et al. (2010); Schindler et al. (2010); Dezayes et al. (2013); Stober and Bucher (2015); Sanjuan et al. (2016); Vidal and Genter (2018); Vidal et al. (2019)
Pannonian Basin	17	Fluvio-lacustrine facies	44 °C–128 °C	Varsányi et al. (1997)
German Molasse Basin	9	Marine facies, Malm	36 °C–153 °C	Ystroem et al. (2022)
Paris Basin	18	Marine facies, Dogger	47 °C–76 °C	Marty et al. (1988); Michard and Bastide (1988); Criaud et al. (1989)
Iceland	79	Basalt, hyaloclastite	59 °C–295 °C	Arnórsson (1977), 1978; Arnórsson et al. (1983); Guðmundsson and Arnórsson (2002); Arnórsson et al. (2007); Óskarsson et al. (2015)
Azores	19	Basalt	200 °C–240 °C	Carvalho et al. (2006)
El Tatio	6	Dacite	180 °C–253 °C	Ellis and Mahon (1977); Giggenbach (1978)
Miravalles	10	Andesite	215 °C–255 °C	Dennis et al. (1989); Gherardi et al. (2002)
Rotorua	10	Rhyolite, andesite	121 °C–211 °C	Mroczek et al. (2003)

1993). They surpass Triassic to Permian sediments, though they are mostly produced from the deeper granitic crystalline basement (Stober and Bucher, 2015; Sanjuan et al., 2016). The Pannonian Basin is a back-arc basin filled with interbedded fluvial and lacustrine sediments. The total dissolved solids (TDS) of the samples are in the range of 1.2–4.4 g/l. The fluids are Na^+-HCO_3^- type (Varsányi et al., 1997). The German Molasse Basin is a foreland basin, where the hosting geothermal reservoirs are Jurassic marine facies, mostly Malm (Birner et al., 2011). The fluid chemistry is varying from a northern Na^+-Ca^{2+}-Mg^{2+}-HCO_3^- type to a more saline southern Na^+-(Ca^{2+})-HCO_3^--Cl^- type (Birner et al., 2011). In the sedimentary Paris Basin, marine Dogger layers are the targeted facies for energy production (Criaud et al., 1989). The Na^+-Ca^{2+}-HCO_3^--Cl^- type fluids show high variability in their salinity (6.4–35 g/l) (Michard and Bastide, 1988). Iceland represents basaltic facies on the mid-ocean ridge induced by a hotspot. The high-enthalpy fields are either fed by meteoric or seawater ranging from a
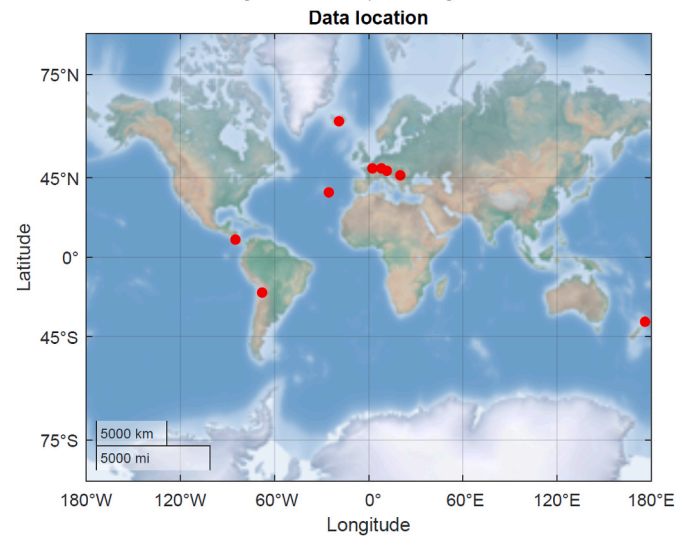

Fig. 1. Location of the acquired data of the seven geothermal sites for training and verifying the ANN geothermometer.

Na^+-HCO_3^--Cl^- to a Na^+-Cl^- type (Arnórsson et al., 1983). Based on these five geothermal fields, AnnRG is established.

To encounter AnnRG in practice, four additional sites of unknown data are aggregated and introduced to the established geothermometer. On the Azores, the geochemical data is from wells drilled in the Água de Pau Massif in the vicinity of the Fogo Volcano. The eruption cycles show a sequence of effusive basaltic to Plinian activity (Carvalho et al., 2006). The TDS varies between 0.07 and 27.1 g/l corresponding to Na^+–HCO_3^- and Na^+–HCO_3^-–Cl^- type waters (Cruz and França, 2006). The subduction zones of the Pacific Ring of Fire are dominated by a broad range of andesite to rhyolite. At El Tatio in Chile, the dacitic reservoir is implemented in an ignimbrite formation resulting in a Na^+-Cl^- type brine in the wells (Ellis and Mahon, 1977; Giggenbach, 1978). The geothermal site in Miravalles, Costa Rica, produces from an andesitic reservoir (Dennis et al., 1989; Gherardi et al., 2002). The downhole fluid samples are neutral Na^+-Cl^- type brines (Grigsby et al., 1989). At Rotorua Geothermal Field in New Zealand, the fluid is in contact with rhyolite and ignimbrite domes within the reservoir (Wood, 1992). The chemistry of the fluid is a Na^+-HCO_3^--Cl^- type (Mroczek et al., 2003).

2.2. Implementation of the dataset and data editing

To set up the dataset, the geochemical analyses of the references are digitised (Table 1). The element concentrations and system parameters of the fluid analyses are compiled into a CSV file. Afterwards, the geochemical dataset is sorted by its count of element concentrations and by the geothermal site. In the next step, the measured *in-situ* temperatures are ascertained from literature (Table 1) and matched to the associated wells. Then, the geochemical dataset and their reservoir temperatures are aggregated. This aggregated dataset is the foundation of the database, which is customised by selecting the required input parameters. Creating the database, intentionally only parameters such as element concentrations of major cations and anions as well as system parameters, like pH value, which are typically comprised in any standard geochemical fluid analysis, are used. This selection increases the data availability, whereas constituent trace elements such as aluminium or lithium, as well as elements with species of different oxidation states such as sulfur and carbon have been excluded. Such parameters are often not measured and therefore, would lead to an incomplete database and a decrease in sample number. As a compromise of sensitivity and availability, the following input parameters are selected: Na^+, K^+, Ca^{2+}, Mg^{2+}, Cl^-, SiO_2, and pH. The sensitivity of temperature to the

concentration of these parameters makes them also essential for conventional solute geothermometry (e.g. Arnórsson 2000b; Fournier and Truesdell 1973; Giggenbach 1988; Nieva and Nieva, 1987; Spycher et al., 2014). Regarding the established parameter selection, the dataset is equalised. All unnecessary parameters are deleted. The distribution of each parameter comprising the data is visualised in Fig. 2.

Statistical data editing is performed to evaluate the dataset. Throughout the dataset, 163 samples are identified representing geothermal fluid from boreholes with measured *in-situ* reservoir temperatures (c.f. Table 1). The data of these samples are stored in matrix $x \in \mathbb{R}\ 163 \times 7$ corresponding to the seven previously selected geochemical input parameters (Na^+, K^+, Ca^{2+}, Mg^{2+}, Cl^-, SiO_2, and pH). In addition, the matrix x is extended by the vector of the associated *in-situ* reservoir temperature $y \in \mathbb{R}\ 163 \times 1$. After the merging, the matrix z contains individual fluid samples in each row while the columns correspond to the geochemical features and the measured *in-situ* temperature. The matrix z is the database for the training of the ANN. Validation is performed to ensure the quality of the database and remove outliers. Therefore, a basic neural network is trained and tested with standardised features. The range of the input parameters is scaled and centred to not bias the net while training. In this regard, the mean of a parameter is subtracted from the value and divided by the standard deviation of the parameter. Afterwards, the temperature predictions are compared to the measured *in-situ* reservoir temperatures. To improve the quality of the database and thus, the accuracy of the ANN, wide reservoir temperature differences have to be removed. To identify these outliers, a threshold criterion is defined as the twofold initial root mean square error (RMSE)

(Equation (1)).

$$2RMSE = 2\sqrt{\frac{\sum_0^{n-1}(y - \widehat{y})^2}{n}} \qquad (1)$$

In the outlier detection, the RMSE shows the average distance between the predicted reservoir temperatures $\widehat{y}$ and the known *in-situ* reservoir temperatures y regarding the sample size n. The results of each sample are given in Fig. 3.

The result of the threshold criterion (Equation (1)) is a temperature deviation of 40.2 K, which is indicated by the dotted black line in Fig. 3. For each sample, the absolute deviation is plotted (blue data points) throughout the database. As a result, eight outliers exceed the threshold value (Fig. 3a). After the outlier removal, the neural network is trained and tested again resulting in a more homogenous deviation distribution, where the new twofold RMSE is 23.8, which is visualised by the dotted green line (Fig. 3b). The database (matrix $z \in \mathbb{R}\ 155 \times 8$) is validated for the establishment of the baseline model of the neural network.

2.3. Baseline model, network architecture, and hyperparameter optimisation

AnnRG is processed in Python 3.8.5 (van Rossum, 1995). Multiple libraries such as *NumPy* for scientific computation (van der Walt et al., 2011; Harris et al., 2020), *pandas* for data analysis (Reback et al., 2020), and *Matplotlib* (Hunter, 2007; Caswell et al., 2020) as well as *seaborn* (Waskom, 2021) for visualisation are used. In addition, *scikit-learn* (Pedregosa et al., 2011), as well as *TensorFlow* (Abadi et al., 2015;
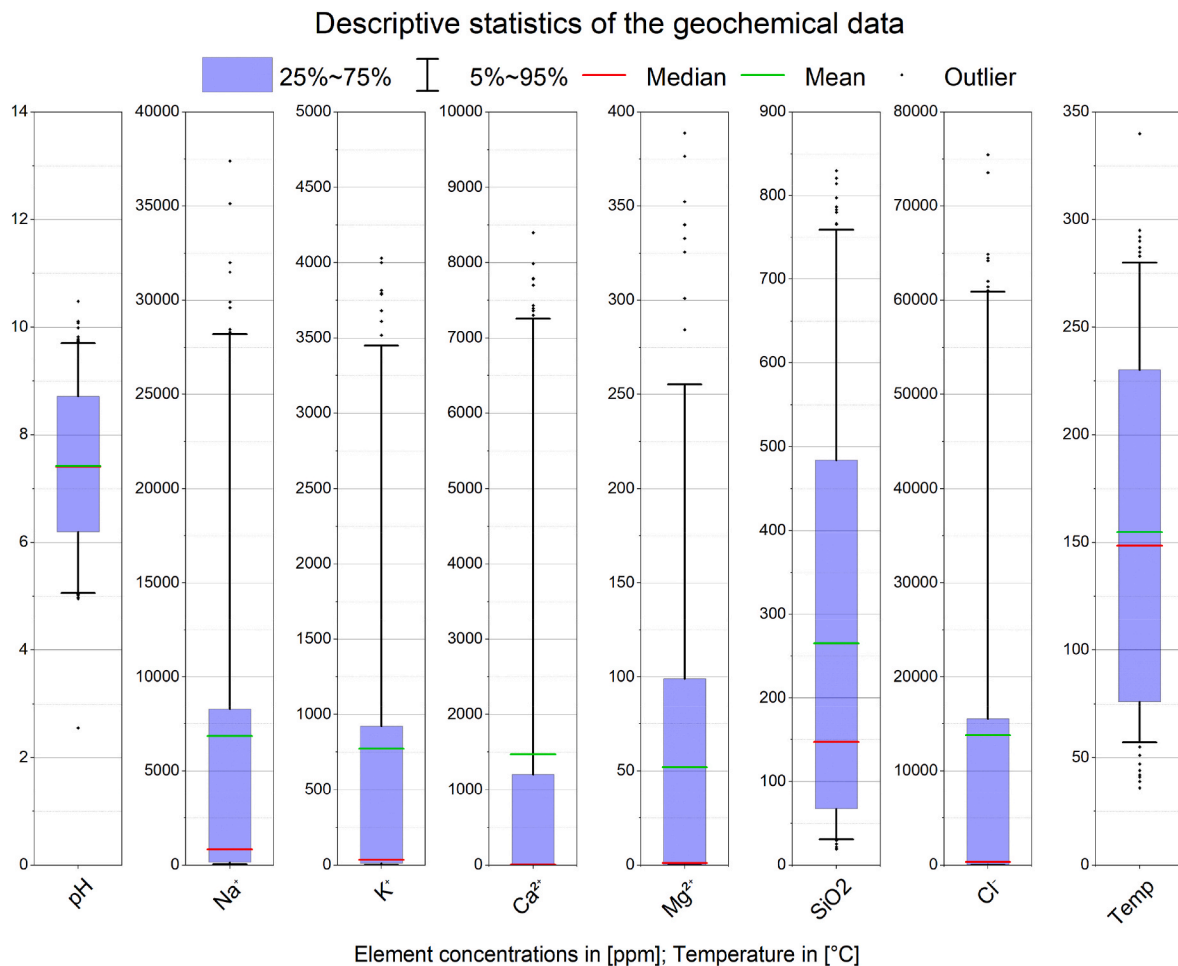

Fig. 2. Parameter distribution of the data compiled from the literature (cf. Table 1) as boxplots, where the median (red line) and the mean (green line) of the dataset are visualised.
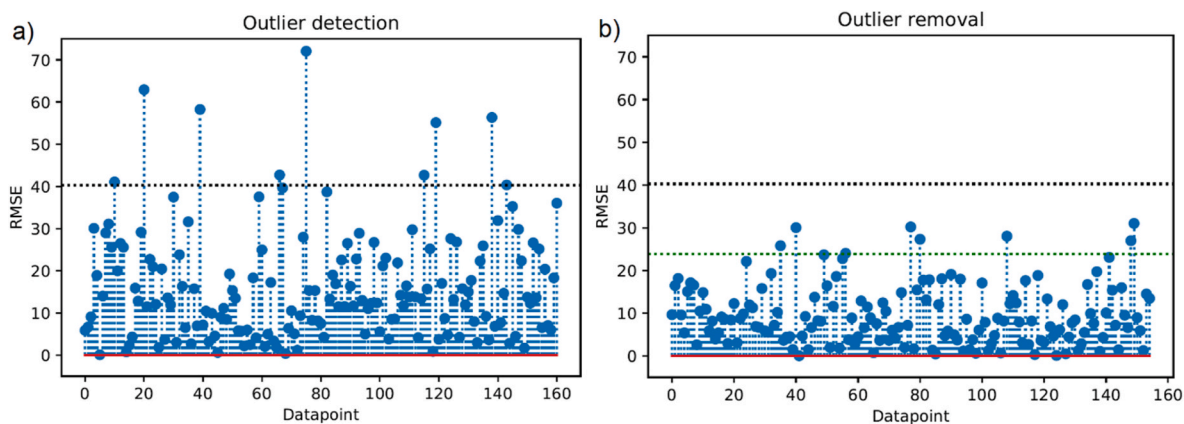
Fig. 3. a) Outlier detection within the dataset. The threshold is defined as twofold root mean square error (RMSE, black dotted line) of the initial predicted temperature difference. b): Dataset after outlier removal with the new twofold RMSE (green dotted line).

TensorFlow Developers, 2022) are used for the ML algorithm. For the latter, the high-level application programming interface *Keras* (Chollet, 2015) runs on top of it.

The data structure of chemical analyses and associated borehole temperatures qualifies the application of a supervised learning approach. A feedforward multilayer perceptron (MLP) is realised for the regression analysis of fluid chemistry and reservoir temperature. This regression problem is given by the function $f : \mathbb{R}^m \rightarrow \mathbb{R}$ fitting multiple parameter m to one scalar output. To train the MLP, the data is split into three groups: 70% training data, 20% validation data, and 10% testing data. This allocation is chosen to train the model properly, while the hyperparameters, which control the model capacity are not overfitted; as well as a separate test set to monitor the generalisation error. To run the code with the same random seed again, the global and the operation seed are set. This seed randomly assigns the data to each group. Hence, the developed networks are comparable and the progress of optimisations can be displayed. To not bias the network, the data is transformed in a centred and scaled manner like aforementioned. During the training, the MLP repeatedly adjusts weights within neurons while minimising the error between the predicted and measured reservoir temperature via gradient descent (Rumelhart et al., 1986). The gradient descent is calculated using back-propagation computing the sum of partial derivatives of the error, which are depending on the weights of the connected neurons throughout the neural net (Graves, 2012). This error surface is searched for its global minimum as the best-fitting result of the network (Rumelhart et al., 1986). As a result, the input parameters are processed within the hidden layer finding learning rules iteratively matching the output data.

The architecture of the neural network is evolved to establish a reasonable baseline model for the development of AnnRG. Afterwards, the baseline model is refined by hyperparameter optimisation minimising the error within the MLP. The data structure and the intrinsic properties of the temperature prediction problem constrain the network architecture. A simple supervised MLP with fully connected layers is chosen. The input layer is given by seven neurons, representing the predefined input parameters. For the output layer, a single neuron is implemented ensuing in the temperature prediction. The adjustment of the network design is coupled to the number of hidden layers as well as the number of neurons within these layers. Starting with this simple baseline model, the architecture design of the network is improved based on validation error minimisation. The number of hidden layers is tested stepwise via *scikit-learn's* GridSearchCV up to 20 layers. Simultaneously, the number of neurons is varied from 10 to 100 in five increments per layer. During the architecture optimisation, Early Stopping (Wahba, 1987; Yao et al., 2007) is used to avoid overfitting the neural net. The patience of GridSearchCV is set to 20 epochs while the MLP is able to perform up to 300 epochs. To solve the regression problem of the

temperature prediction, different activation functions were tested: the rectified linear unit (ReLu) (Jarrett et al., 2009), sigmoid function, and softmax. As a result, the best-fitting architecture is achieved with one hidden layer, 80 neurons, and ReLu as the activation function. The measured performance of the established network has a coefficient of determination (R^2) > 0.9, which is acceptable to continue the optimisation. The developed architecture design is used for further refinement of the hyperparameters.

In order to optimise the hyperparameter, multiple parameters were selected and stepwise analysed using *scikit-learn's* GridSearchCV. Overall, the network is trained while using Early Stopping to prevent overfitting. The patience is set to 20 epochs, before the GridSearchCV is active, while the MLP is able to perform up to 300 epochs. The optimisers, as well as their learning rate and batch size, were analysed interdependently. In the case of *Keras'* optimisers, adaptive moment estimation (Adam) (Kingma and Ba, 2014), stochastic gradient descent (SGD) (Sutskever et al., 2013), as well as root mean square propagation (RMSprop) (Tieleman and Hinton, 2012) were compared. To fit the model to an optimal effective capacity, the learning rate within the optimisers is varied from 10^{-4} to 10^{-1} increasing by half an order of magnitude per step. The batch size is varied from 1 up to 32 in 2^n steps. All parameters are varied interdependently to lower the generalisation error while matching the training error. The training error, validation error, and testing error are monitored. The errors of the best-fitting MLP are presented in Table 2.

The three error types are chosen due to their inherent information in the regression analysis. In Equation (2), the mean absolute percentage error (MAPE) indicates the precision of the regression function and its multiple input parameter m to its output $f : \mathbb{R}^m \rightarrow \mathbb{R}$, where $\hat{y}$ is the predicted reservoir temperature, y is the known *in-situ* reservoir temperature, and n is the sample size.

$$\text{MAPE} = \frac{1}{n} \sum_{0}^{n-1} \frac{y - \hat{y}}{|\hat{y}|} \tag{2}$$

The RMSE defines the average accuracy between the predicted and the in-situ temperature (Equation (3)).

Table 2
Illustration of three error types of the best-fitting MLP. The mean absolute percentage error (MAPE), the root mean square error (RMSE), and R^2 are given for the training, validation, and testing of the neural net.

Error type	Training	Validation	Testing
MAPE	0.067	0.092	0.092
RMSE	9.965	11.269	10.091
R^2	0.983	0.972	0.978

$$RMSE = \sqrt{\frac{\sum_0^{n-1}(y-\widehat{y})^2}{n}} \tag{3}$$

The R^2 shows how accurately the model predicts the measured in-situ temperatures (Equation (4)).

$$R^2 = 1 - \frac{\sum_1^n (y-\widehat{y})^2}{\sum_1^n \left(y - \left(\frac{1}{n}\sum_1^n y\right)\right)^2} \tag{4}$$

These errors are given for all three phases of training, validating, and testing the neural net. In addition, the shape of the loss function is visualised as learning curves in Fig. 4.

The learning curves of the training phase (blue line) and the validation phase (orange line) are plotted over the epochs of the MLP. The error minimisation of the loss function is illustrated by the mean square error. Regarding Fig. 4, the Early Stopping function fixed the weights of the 142 epoch resulting in the best hyperparameter configuration of the predefined network architecture. As a result of the GridSearch CV, the activation function Adam (Kingma and Ba, 2014) with a learning rate of 10^{-3} and a batch size of 16 is fitting the regression problem of temperature estimation best. These hyperparameters are further used for AnnRG.

3. Results & discussion

After the establishment of the neural network architecture and the hyperparameter configuration, the final MLP (Fig. 5) is given by the following configuration (Table 3):

One input layer with seven neurons, representing the input parameters (Na^+, K^+, Ca^{2+}, Mg^{2+}, Cl^-, SiO_2, and pH), one hidden layer with 80 neurons, and the output layer with one neuron representing the reservoir temperature prediction. The layers are fully connected with ReLu as the activation function and Adam as the optimiser. For the hyperparameter optimisation, a learning rate of 10^{-3} and a batch size of 16 is fitting the best, when the net is trained with Early Stopping (patience 20, and up to 300 epochs). Regarding the sufficient sample size of the dataset ($z \in \mathbb{R}\,155 \times 8$), this shallow network is less prone to overfitting compared to a deep neural network. This also corresponds to the errors while establishing the net (Table 2). The MAPE of the training (0.067), validation (0.092), and testing (0.092) show a close correlation between the input parameters and the regression problem. The slight increase in the MAPE from the training phase to the validation and testing phase is the result of the data splitting (70% training, 20% validation, and 10%
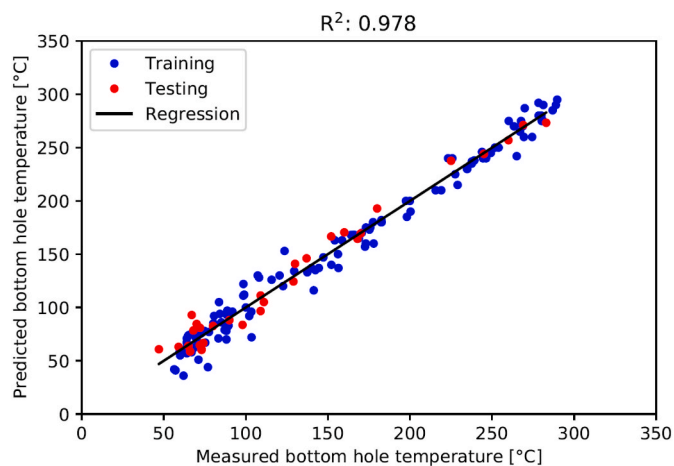

Fig. 5. Result of the predicted temperature against the measured in-situ temperature with $R^2 = 0.978$. The training data (blue points) and testing data (red points) are visualised with the regression line (black line, $R^2 = 1$).

testing) and therefore, the stepwise decrease in data. The low deviation of the RMSE for the three phases displays a good accuracy amongst predicted and measured temperatures on average. The variance of 1.304 from training to validation, as well as the variance of -1.178 from validation to testing, is in the order of randomisation of the data. In addition, the deviation of their R^2 values is also marginal representing a well-established model. Thus, the accuracy of the temperature prediction is comparable for each step. These results also correspond to the learning curves (Fig. 4). The smooth shape of the validation curve implies an appropriate tuning of the hyperparameters fitting the model. The close distance between the validation and training curve equals a small generalisation gap implying a well-balanced model capacity.

In Fig. 5, the results of the regression problem of the temperature prediction are visualised for the best-fitting MLP. The coloured dots illustrate the actual results of the training (blue), the testing (red), and their deviation of the regression line (cf. Fig. 6). The homogeneous distribution of the dots, as well as an R^2 of 0.978, approve the developed MLP.

In Fig. 6, the overall error distribution of the dataset is displayed as a kernel density plot. It visualises the probability density of a random temperature prediction based on the weights. Hence, the curve comprises the positive and negative deviation of each temperature prediction in comparison to the measured reservoir temperature. The shape of the distribution has a slight positive skewness, implying a minor underprediction of the reservoir temperature. In addition, a box plot gives the axis of symmetry. The maximum temperature differences are ±30 K in each case for two samples. The median is 1.9 K where the box has also a slight positive overhang implying a marginal over-prediction of the reservoir temperature. The interquartile range (IQR) of 17.3 K also shows the accuracy of AnnRG. To investigate the results of the testing phase, the testing error is decoupled and plotted as a histogram in Fig. 7.

The error histogram of the test set (31 samples) is distributed between -18 and 22 K, which is more precise than the overall error distribution of the dataset (Fig. 6). In line with the positive skewness of the error distribution (Fig. 6), the temperature predictions of the test set are minorly underestimate the temperature. To verify AnnRG and encounter the established geothermometer in practice, the geothermometer was applied to unknown data from other geothermal systems: The Azores, Portugal; El Tatio, Chile; Miravalles, Costa Rica; and Rotorua, New Zealand (Table 1). The geochemical data of these four geothermal sites are processed by the MLP and compared with the measured *in-situ* temperatures. In Fig. 8, the results of each site are plotted on top of the developed geothermometer.

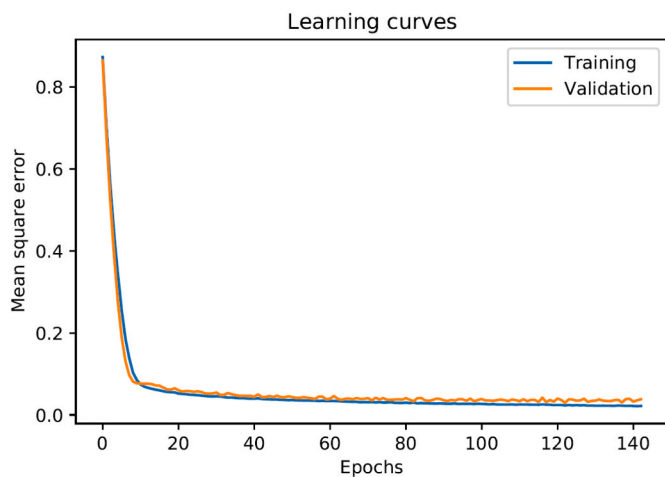The predicted temperatures of all four sites (Fig. 8) fit the measured

Fig. 4. Learning curves of the training (blue line) and the validation (orange line) of the ANN. The Cross-entropy loss is visualised against the epochs until the Early Stopping function completes the learning phase.

Table 3
Final network architecture and hyperparameter configuration of AnnRG.

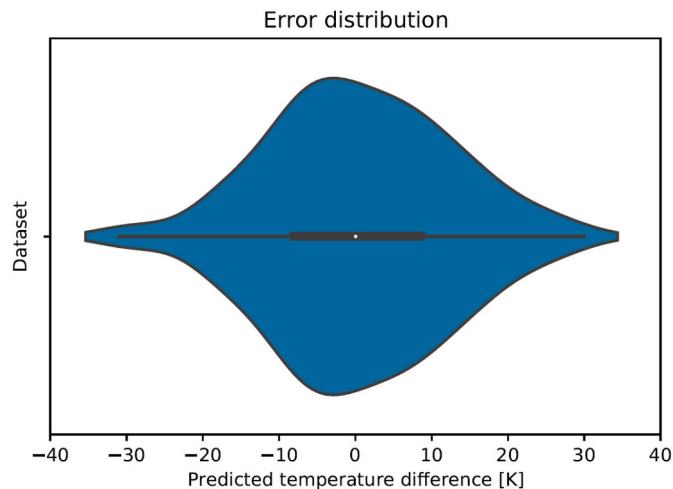| Layers	Neurons	Activation	Optimiser	Learning rate	Batch size	Metrics	Losses
Input layer	7	ReLu	Adam	10^{-3}	16	RMSE	MSE
Hidden layer	80					MAPE	
Output layer	1					R^2	

Fig. 6. Error distribution of the temperature difference in kelvins between the predicted and measured temperature of the entire dataset.
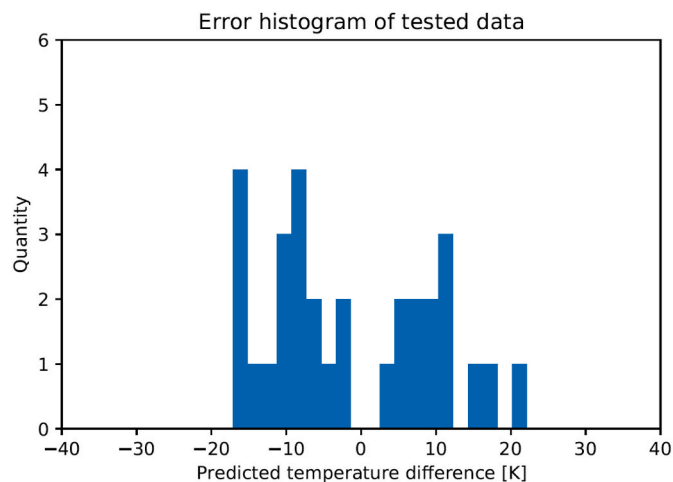

Fig. 7. Error histogram of the temperature difference in kelvins between the predicted and measured temperature of the test dataset.

temperatures in the same order of $<\pm30$ K as the MLP error distribution (Fig. 6). The error distribution of each sample is visualised in Fig. 9. Especially for the Azores (±11 K), El Tatio (±13 K), and Miravalles (±15 K), the predictions are more precise than the error distribution of the test set (Fig. 7). Nevertheless, the variation between measured and predicted temperatures at Rotorua (±27 K) is higher than the average test error but lower than the overall error distribution. In summary, the introduction of unknown data to the trained MLP verifies the applicability of AnnRG.

As mentioned in the introduction, the predictions of an ANN are sensitive to the size of the dataset. To evaluate the sufficiency of data pairs, a sensitivity analysis of the sample size of the database is conducted. The validated database is successively reduced in its sample size. In each iteration, the dataset is randomly reduced by one sample and the

MLP is trained again with the same model parameters. The R^2 of each recalculation is plotted over the remaining sample size (Fig. 10).

The results of the R^2 score (black dots) are fitted by an exponential decay function (red line). For a sample size between 155 and 65, the R^2 is varying between 0.911 and 0.987. This spread is attributable to the random incremental reduction of the sample size, while the seed of the database is fixed. Therefore, the samples within the batches are reallocated, which means that the same amount of data is used to train the MLP in every iteration. The R^2 score declines exponentially with a sample size of less than 65 and reaches 0.365 at 58 samples. In conclusion, a sufficient sample size (>65) is required to obtain a suitable database to train, validate, and test the MLP.

4. Conclusion

Up to now, due to typical limited data density and availability the application of ML approaches in geochemistry is very rare. Herein, for the first time, a unique dataset of 208 samples is compiled as the basis for the development of the first adequate solute ANN geothermometer, called AnnRG. This data comprises measured hydrochemical fluid data and corresponding measured *in-situ* temperature from a broad variety of geological settings with high complexity in fluid chemistry (Table 1). The MLP is suitable for processing such heterogeneous data resulting from complex thermodynamic processes of subsurface water-rock interaction. AnnRG is built upon the evaluation of element concentrations and ratios similar to conventional geothermometry. Moreover, the tool performs a multi-parameter analysis training itself without explicitly programming the tool. In contrast to automated and numerical optimised multicomponent geothermometers, no implementation of sophisticated optimisation processes, or adaptation of the reservoir mineral assemblage is needed. In addition, AnnRG evaluates data more efficiently in a timely and computationally manner. Nevertheless, the development of AnnRG is sensitive to the size of the dataset. Regarding this issue, a data size sensitivity analysis was conducted. As a result, >65 data pairs are a sufficient sample size still yielding precise prediction accuracy. Fortunately, nowadays there is a continuous increase in geochemical data, which can be compiled by enhancing the database and improving AnnRG.

For AnnRG a standard geochemical fluid analysis comprising system parameters and major element concentration (Na^+, K^+, Ca^{2+}, Mg^{2+}, Cl^-, SiO_2, and pH) is sufficient to predict reservoir temperatures without the need to sample and analyse trace elements, isotopes, or gas phases. After the removal of eight outliers, 155 data pairs are used to train the tool. Then, the applicability and accuracy of the geothermometer are tested on 61 samples comprising 45 samples of new unknown data from four different geothermal fields worldwide. The applicability of the trained MLP is successfully verified resulting in a similar average accuracy (RMSE 9.405) than the original dataset (10.442). AnnRG is applicable to regional-scale sites independent of geological settings. In addition, this application leads to less error propagation than approaches with predicted reservoir temperatures as input parameters. Eventually, the optimisation of the network architecture as well as the hyperparameters continuously improves the geothermometer throughout its development. AnnRG provides precise reservoir temperature predictions with an IQR of 17.3 K. In addition, the geothermometer has a high prediction accuracy of $R^2 = 0.978$. Overall, the implementation and verification of AnnRG is an advancement in solute geothermometry showing that ML can identify coherencies between hydrochemical data and temperature.
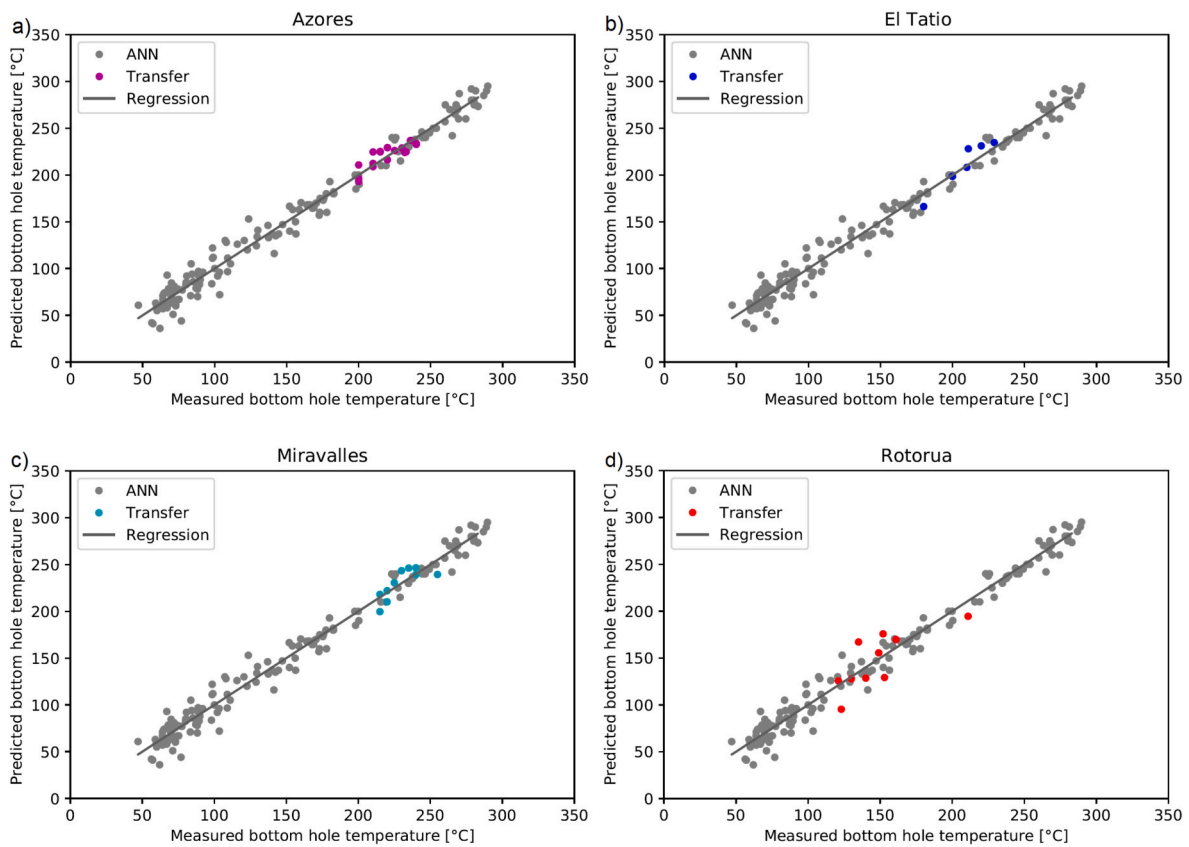
Fig. 8. The introduction of AnnRG to unknown data: a) Azores, Portugal b) El Tatio, Chile c) Miravalles, Costa Rica, d) Rotorua, New Zealand (c.f. Table 1). The data (grey points) are visualised with the regression line (grey line, $R^2 = 1$) and the results of the transferred data (coloured points).
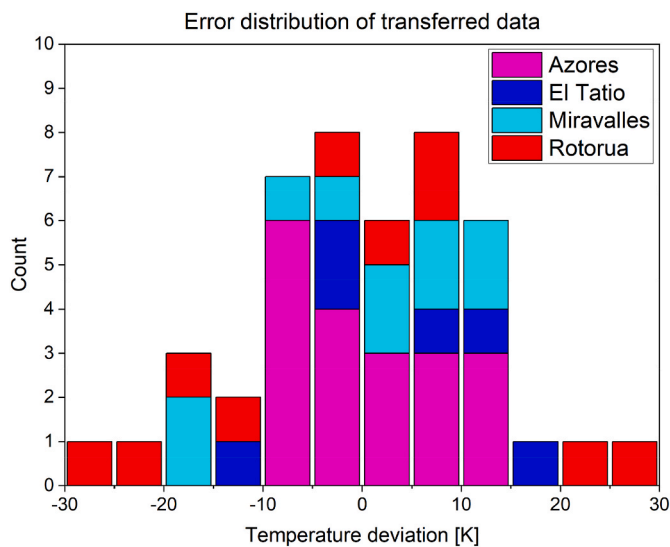

Fig. 9. Error distribution of the introduced data with a batch size of 5 K. Count of the samples against the temperature deviation of Azores, Portugal (magenta); El Tatio, Chile (blue); Miravalles, Costa Rica (cyan); Rotorua, New Zealand (red).

Fig. 10. Sensitivity analysis of the sample size of the database. The R^2 is calculated stepwise reducing one random sample at a time. The distribution of the R^2 (black dots) is fitted by a curve of exponential decay (red curve).

Moreover, the potential for further development regarding new applications in geochemistry and increasing data size is vast. In the future, more advanced statistical evaluation regarding algorithms or optimisations may further enhance the accuracy of ML in geochemistry.
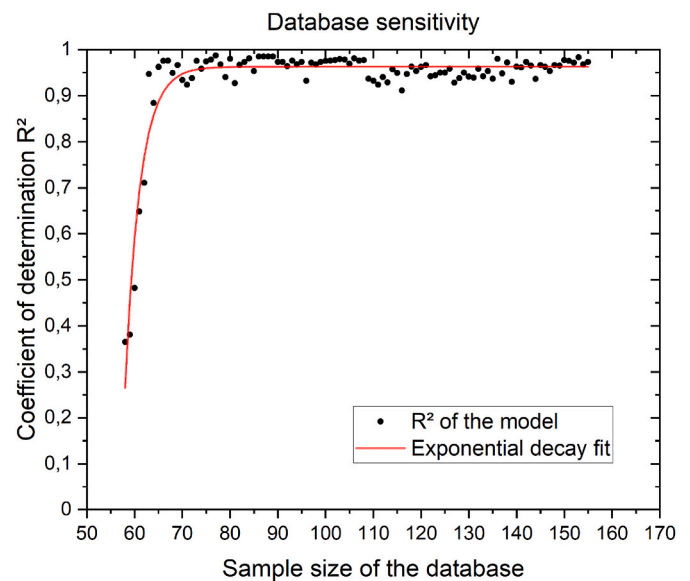
Authorship statement

Lars Ystroem: Conceptualisation, Data curation, Investigation, Methodology, Software, Writing - Original Draft. Mark Vollmer: Data curation, Methodology, Software. Thomas Kohl: Writing - Review & Editing, Supervision. Fabian Nitschke: Conceptualisation, Writing -

Review & Editing, Supervision, Funding acquisition.

CRediT authorship contribution statement

Lars H. Ystroem: Writing – original draft, Visualization, Validation, Software, Methodology, Investigation, Data curation, Conceptualization. **Mark Vollmer:** Software, Methodology, Investigation, Conceptualization. **Thomas Kohl:** Writing – review & editing, Supervision, Funding acquisition, Conceptualization. **Fabian Nitschke:** Writing – review & editing, Supervision, Project administration, Investigation, Funding acquisition, Conceptualization.

Declaration of competing interest

The authors declare that they have no known competing financial interests or personal relationships that could have appeared to influence the work reported in this paper.

Data availability

All data is cited within the manuscript.

Acknowledgement

References

Abadi, M., Agarwal, A., Barham, P., Brevdo, E., Chen, Z., Citro, C., Corrado, G.S., Davis, A., Dean, J., Devin, M., Ghemawat, S., Goodfellow, I., Harp, A., Irving, G., Isard, M., Jia, Y., Jozefowicz, R., Kaiser, L., Kudlur, M., Levenberg, J., Mane, D., Monga, R., Moore, S., Murray, D., Olah, C., Schuster, M., Shlens, J., Steiner, B., Sutskever, I., Talwar, K., Tucker, P., Vanhoucke, V., Vasudevan, V., Viegas, F., Vinyals, O., Warden, P., Wattenberg, M., Wicke, M., Yu, Y., Zheng, X., 2015. TensorFlow: Large-Scale Machine Learning on Heterogeneous Distributed Systems 172. CoRR. http://arxiv.org/pdf/1603.04467v2.

Altay, O., Altay, E.V., 2023. A novel hybrid multilayer perceptron neural network with improved grey wolf optimizer. Neural Comput. Appl. 35, 529–556.

Altay, E.V., Gurgenc, E., Altay, O., Dikici, A., 2022. Hybrid artificial neural network based on a metaheuristic optimization algorithm for the prediction of reservoir temperature using hydrogeochemical data of different geothermal areas in Anatolia (Turkey). Geothermics 104, 102476.

Aquilina, L., Pauwels, H., Genter, A., Fouillac, C., 1997. Water-rock interaction processes in the Triassic sandstone and the granitic basement of the Rhine Graben: geochemical investigation of a geothermal reservoir. Geochem. Cosmochim. Acta 61, 4281–4295.

Arnórsson, S., 1977. Changes in the Chemistry of Water and Steam Discharged from Wells in the Námafjall Geothermal Field, Iceland, during the Period 1970–76. JÖKULL, pp. 47–59.

Arnórsson, S., 1978. Major element chemistry of the geothermal sea-water at Reykjanes and Svartsengi, Iceland. Mineral. Mag. 42, 209–220.

Arnórsson, S. (Ed.), 2000a. Isotopic and Chemical Techniques in Geothermal Exploration, Development and Use: Sampling Methods, Data Handling, Interpretation. International Atomic Energy Agency, Vienna, p. 351.

Arnórsson, S., 2000b. The quartz- and Na/K geothermometers: I. New thermodynamic calibration. In: Proceedings World Geothermal Congress: Kyushu-Tohoku, Japan, pp. 929–934.

Arnórsson, S., Sigurdsson, S., Svavarsson, H., 1982. The chemistry of geothermal waters in Iceland. I. Calculation of aqueous speciation from 0° to 370°C. Geochem. Cosmochim. Acta 46, 1513–1532.

Arnórsson, S., Gunnlaugsson, E., Svavarsson, H., 1983. The chemistry of geothermal waters in Iceland. II. Mineral equilibria and independent variables controlling water compositions. Geochem. Cosmochim. Acta 47, 547–566.

Arnórsson, S., Stefánsson, A., Bjarnason, J.O., 2007. Fluid-fluid interactions in geothermal systems. Rev. Mineral. Geochem. 65, 259–312.

Birner, J., Mayr, C., Thomas, L., Schneider, M., Baumann, T., Winkler, A., 2011. Hydrochemie und Genese der tiefen Grundwässer des Malmaquifers im bayerischen Teil des süddeutschen Molassebeckens. Z. Geol. Wiss. 39, 291–308.

Bjarnason, J.Ö., 2010. WATCH: the Chemical Speciation Program. ÍSOR – Iceland Geosurvey, Reykjavík, Iceland.

Can, I., 2002. A new improved Na/K geothermometer by artificial neural networks. Geothermics 31, 751–760.

Carvalho, M.R., Forjaz, V.H., Almeida, C., 2006. Chemical composition of deep hydrothermal fluids in the Ribeira Grande geothermal field (São Miguel, Azores). J. Volcanol. Geoth. Res. 156, 116–134.

Caswell, T.A., Droettboom, Michael, Lee, Antony, Hunter, John, Sales de Andrade, Elliott, Firing, Eric, Hoffmann, Tim, Klymak, Jody, Stansby, David, Varoquaux, Nelle, Nielsen, Jens Hedegaard, Root, Benjamin, May, Ryan, Elson, Phil, Seppänen, Jouni K., Dale, Darren, Lee, Jae-Joon, McDougall, Damon, Straw, Andrew, Hobson, Paul, Gohlke, Christoph, S Yu, Tony, Ma, Eric, Vincent, Adrien F., Silvester, Steven, Moad, Charlie, Kniazev, Nikita, hannah, Ernest, Elan, Ivanov, Paul, 2020. Matplotlib/Matplotlib: REL: v3.3.2. Zenodo.

Chollet, F., 2015. Keras.

Criaud, A., Fouillac, C., Marty, B., 1989. Low enthalpy geothermal fluids from the Paris Basin - 2 Oxidation-reduction state and consequences for the prediction of corrosion and sulfide scaling. Geothermics 18.

Cruz, J.V., França, Z., 2006. Hydrogeochemistry of thermal and mineral water springs of the Azores archipelago (Portugal). J. Volcanol. Geoth. Res. 151, 382–398.

Davies, C.W., 1938. The extent of dissociation of salts in water. Part VIII.: an equation for the mean ionic activity coefficient of an electrolyte in water, and a revision of the dissociation constants of some sulphates. J. Chem. Soc. 2093–2098, 397.

Debye, P., Hückel, E., 1923. Zur Theorie der Elektrolyte: 1. Gefrierpunktserniedrigung und verwandte Erscheinungen. Phys. Z. 24, 185–206.

Dennis, B.R., Lawton, R.G., Kolar, J.D., Alvarado, A., 1989. Results of Investigation at the Miravalles Geothermal Field, Costa Rica Part 1: Well Logging: LA-1510-MS, Part 1. Los Alamos National Laboratory.

TensorFlow Developers, 2022. TensorFlow. Zenodo. https://doi.org/10.5281/zenodo.4758419.

Dezayes, C., Sanjuan, B., Gal, F., Lerouge, C., Brach, M., 2013. Forage d'exploration géothermique GRT1: suivi géochimique des fluides et caractérisation des zones fracturées. In: Rapport Final. BRGM/RP - 62546-FR.

Díaz-González, L., Santoyo, E., Reyes-Reyes, J., 2008. Tres nuevos geotermómetros mejorados de Na/K usando herramientas computacionales y geoquimiométricas: aplicación a la predicción de temperaturas de sistemas geotérmicos, vol. 25, pp. 465–482.

Ellis, A.J., 1963. The solubility of calcite in sodium chloride solutions at high temperatures. Am. J. Sci. 261, 259–267.

Ellis, A.J., Mahon, W., 1964. Natural hydrothermal systems and experimental hot-water/rock interactions. Geochem. Cosmochim. Acta 28, 1323–1357.

Ellis, A.J., Mahon, W.A.J., 1977. Chemistry and Geothermal Systems. Academic Press, New York, p. 392.

Ferhat Bayram, A., 2001. Application of an artificial neural network model to a Na–K geothermometer. J. Volcanol. Geoth. Res. 112, 75–81.

Fournier, R.O., 1977. Chemical geothermometers and mixing models for geothermal systems. Geothermics 5, 41–50.

Fournier, R.O., Potter, R.W., 1979. Magnesium correction to the Na-K-Ca chemical geothermometer. Geochem. Cosmochim. Acta 43, 1543–1550.

Fournier, R.O., Potter, R.W., 1982. Revised and expanded silica (quartz) geothermometer. Bull., Geotherm. Resour. Counc. (Davis, Calif.); (United States) 11, 10.

Fournier, R.O., Rowe, J.J., 1966. Estimation of underground temperatures from the silica content of water from hot springs and wet-steam wells. Am. J. Sci. 264, 685–697.

Fournier, R.O., Truesdell, A.H., 1973. An empirical Na-K-Ca geothermometer for natural waters. Geochem. Cosmochim. Acta 37, 1255–1275.

Fournier, R.O., Truesdell, A.H., 1974. Geochemical indicators of subsurface temperature - Part 2, Estimation of temperature and fraction of hot water mixed with cold water. J. Res. U. S. Geol. Surv. 263–270.

Gherardi, F., Panichi, C., Yock, A., Gerardo-Abaya, J., 2002. Geochemistry of the surface and deep fluids of the Miravalles volcano geothermal system (Costa Rica). Geothermics 31, 91–128.

Giggenbach, W.F., 1978. The isotopic composition of waters from the El Tatio geothermal field, Northern Chile. Geochem. Cosmochim. Acta 42, 979–988.

Giggenbach, W.F., 1981. Geothermal mineral equilibria. Geochem. Cosmochim. Acta 45, 393–410.

Giggenbach, W.F., 1988. Geothermal solute equilibria. Derivation of Na-K-Mg-Ca geoindicators. Geochem. Cosmochim. Acta 52, 2749–2765.

Goodfellow, I., Bengio, Y., Courville, A., 2016. Deep Learning. The MIT Press, Cambridge, Massachusetts, London, England, p. 775.

Graves, A., 2012. Supervised Sequence Labelling with Recurrent Neural Networks. Springer, Berlin, p. 141.

Grigsby, C.O., Goff, F., Trujillo JR., P.E., Counce, D.A., Dennis, B., Kolar, J., Corrales, R., 1989. Results of investigation at the Miravalles geothermal field, Costa Rica. In: Resultados de las investigaciones en el campo geotermico de Miravalles, Costa Rica; Parte 2. Muestreo de fluidos pozo abajo.

Guðmundsson, B.T., Arnórsson, S., 2002. Geochemical monitoring of the Krafla and Námafjall geothermal areas, N-Iceland. Geothermics 31, 195–243.

Haklidir, F.S.T., Haklidir, M., 2020. Prediction of reservoir temperatures using hydrogeochemical data, western Anatolia geothermal systems (Turkey): a machine learning approach. Nat. Resour. Res. 29, 2333–2346.

Harris, C.R., Millman, K.J., van der Walt, S.J., Gommers, R., Virtanen, P., Cournapeau, D., Wieser, E., Taylor, J., Berg, S., Smith, N.J., Kern, R., Picus, M., Hoyer, S., van Kerkwijk, M.H., Brett, M., Haldane, A., Del Río, J.F., Wiebe, M., Peterson, P., Gérard-Marchant, P., Sheppard, K., Reddy, T., Weckesser, W., Abbasi, H., Gohlke, C., Oliphant, T.E., 2020. Array programming with NumPy. Nature 585, 357–362.

Hunter, J.D., 2007. Matplotlib: a 2D graphics environment. Comput. Sci. Eng. 9, 90–95.

Ibrahim, B., Konduah, J.O., Ahenkorah, I., 2023. Predicting reservoir temperature of geothermal systems in Western Anatolia, Turkey: a focus on predictive performance and explainability of machine learning models. Geothermics 112, 102727.

Jarrett, K., Kavukcuoglu, K., Ranzato, M.A., LeCun, Y., 2009. What is the best multi-stage architecture for object recognition?. In: 2009 IEEE 12th International Conference on Computer Vision. 2009 IEEE 12th International Conference on Computer Vision (ICCV), Kyoto. 29.09.2009. IEEE, pp. 2146–2153.

Kingma, D.P., Ba, J., 2014. Adam: A Method for Stochastic Optimization.

Lundberg, S.M., Lee, S.-I., 2017. A unified approach to interpreting model predictions. Adv. Neural Inf. Process. Syst. 30.

Marty, B., Criaud, A., Fouillac, C., 1988. Low enthalpy geothermal fluids from the Paris sedimentary basin - 1 Characteristics and origin of gases. Geothermics 17, 619–633.

Michard, G., Bastide, J.-P., 1988. Etude géochimique de la nappe du dogger du bassin parisien. J. Volcanol. Geoth. Res. 35, 151–163.

Mroczek, E.K., Stewart, M.K., Scott, B.J., 2003. Chemistry of the Rotorua Geothermal Field Part 2: Discharging Wells-update of Chemical and Isotopic Compositions and Comparison with Historical Data.

Nitschke, F., Held, S., Villalon, I., Neumann, T., Kohl, T., 2017. Assessment of performance and parameter sensitivity of multicomponent geothermometry applied to a medium enthalpy geothermal system. Geotherm Energy 5, 1.

Nieva, D., Nieva, R., 1987. Developments in geothermal energy in Mexico - part twelve. A cationic geothermometer for prospecting of geothermal resources. Heat Recov. Syst. CHP 7, 243–258.

Nitschke, F., Held, S., Neumann, T., Kohl, T., 2018. Geochemical characterization of the Villarrica geothermal system, Southern Chile, part II: site-specific re-evaluation of SiO2 and Na-K solute geothermometers. Geothermics 74, 217–225.

Olguín-Martínez, M.G., Peiffer, L., Dobson, P.F., Spycher, N., Inguaggiato, C., Wanner, C., Hoyos, A., Wurl, J., Makovsky, K., Ruiz-Aguilar, D., 2022. PyGeoT: a tool to automate mineral selection for multicomponent geothermometry. Geothermics 104, 102467.

Óskarsson, F., Fridriksson, T., Thorbjörnsson, D., 2015. Geochemical monitoring of the Reykjanes geothermal reservoir 2003 to 2013. In: World Geothermal Congress 2015.

Palmer, C.D., 2014. Reservoir Temperature Estimator (RTEst): User Manual, p. 10.

Palmer, C.D., Ohly, S.R., Smith, R.W., Neupane, G., McLing, T., Mattson, E., 2014. Mineral selection for multicomponent equilibrium geothermometry. GRC Trans. 453–460.

Pang, Z.-H., 1988. Multiple Fluid - Mineral Equilibrium Calculations and Their Applications to Geothermometry and Hydrochemical Processes in Geothermal Systems.

Pang, Z.-H., Reed, M.H., 1998. Theoretical chemical thermometry on geothermal waters: problems and methods. Geochem. Cosmochim. Acta 62, 1083–1091.

Pauwels, H., Fouillac, C., Fouillac, A.-M., 1993. Chemistry and isotopes of deep geothermal saline fluids in the Upper Rhine Graben: origin of compounds and water-rock interactions. Geochem. Cosmochim. Acta 57, 2737–2749.

Pedregosa, F., Varoquaux, Gaël, Gramfort, Alexandre, Michel, Vincent, Bertrand, Thirion, Grisel, Olivier, Blondel, Mathieu, Peter, Prettenhofer, Weiss, Ron, Vincent, Dubourg, Vanderplas, Jake, Alexandre Passos, Cournapeau, David, Brucher, Matthieu, Perrot, Matthieu, Duchesnay, Édouard, 2011. Scikit-learn: machine learning in Python. J. Mach. Learn. Res. 12, 2825–2830.

Pérez-Zárate, D., Santoyo, E., Acevedo-Anicasio, A., Díaz-González, L., García-López, C., 2019. Evaluation of artificial neural networks for the prediction of deep reservoir temperatures using the gas-phase composition of geothermal fluids. Comput. Geosci. 129, 49–68.

Reback, J., McKinney, Wes, jbrockmendel, Van den Bossche, Joris, Augspurger, Tom, Cloud, Phillip, gfyoung, Sinhrks, Hawkins, Simon, Klein, Adam, Roeschke, Matthew, Tratner, Jeff, Petersen, Terji, She, Chang, Ayd, William, MomIsBestFriend, Garcia, Marc, Schendel, Jeremy, Hayden, Andy, Saxton, Daniel, Jancauskas, Vytautas, McMaster, Ali, Battiston, Pietro, Seabold, Skipper, , chris-b1, h-vetinari, Dong, Kaiqi, Hoyer, Stephan, Overmeire, Wouter, Winkel, Martin, 2020. Pandas-Dev/pandas: Pandas 1.1.3. Zenodo.

Reed, M.H., Spycher, N., 1984. Calculation of pH and mineral equilibria in hydrothermal waters with application to geothermometry and studies of boiling and dilution. Geochem. Cosmochim. Acta 48, 1479–1492.

Reichstein, M., Camps-Valls, G., Stevens, B., Jung, M., Denzler, J., Carvalhais, N., Prabhat, 2019. Deep learning and process understanding for data-driven Earth system science. Nature 566, 195–204.

Rumelhart, D.E., Hinton, G.E., Williams, R.J., 1986. Learning representations by back-propagating errors. Nature 323, 533–536.

Sanjuan, B., Jacquot, E., Guigues, N., Foucher, J.-C., Brach, M., Braibant, G., 2001. Field Geochemistry Contribution, Annex 2 (BRGM Contribution) of the Final EEC Report (European Hot Dry Rock Geothermal Research Programme April 1998–June 2001) JOR3-CT98-0313.

Sanjuan, B., Rose, P., Foucher, J.-C., Brach, M., Braibant, G., 2004. Tracer Testing at Soultz-Sous-Forêts (France) Using Na-Benzoate, 1,5 and 2,7-naphthalene Disulfonate. Twenty-Ninth Workshop on Geothermal Reservoir Engineering, p. 8.

Sanjuan, B., Pinault, J.-L., Rose, P., Gérard, A., Brach, M., Braibant, G., Crouzet, C., Foucher, J.-C., Gautier, A., Touzelet, S., 2006. Geochemical Fluid Characterisatics and Main Achievements about Tracer Tests at Soultz-Sous-Forêts (France). BRGM/RP-54776-FR, p. 64.

Sanjuan, B., Millot, R., Dezayes, C., Brach, M., 2010. Main characteristics of the deep geothermal brine (5km) at Soultz-sous-Forêts (France) determined using geochemical and tracer test data. Compt. Rendus Geosci. 342, 546–559.

Sanjuan, B., Millot, R., Innocent, C., Dezayes, C., Scheiber, J., Brach, M., 2016. Major geochemical characteristics of geothermal brines from the Upper Rhine Graben granitic basement with constraints on temperature and circulation. Chem. Geol. 428, 27–47.

Schindler, M., Baumgärtner, J., Gandy, T., Hauffe, P., Hettkamp, T., Menzel, H., Penzkofer, P., Teza, D., Tischner, T., Wahl, G., 2010. Successful Hydraulic Stimulation Techniques for Electric Power Production in the Upper Rhine Graben, Central Europe.

Spycher, N., Finsterle, S., 2016. iGeoT v1.0: Automatic Parameter Estimation for Multicomponent Geothermometry: User's Guide.

Spycher, N., Peiffer, L., Sonnenthal, E.L., Saldi, G., Reed, M.H., Kennedy, B.M., 2014. Integrated multicomponent solute geothermometry. Geothermics 51, 113–123.

Stober, I., Bucher, K., 2015. Hydraulic and hydrochemical properties of deep sedimentary reservoirs of the Upper Rhine Graben, Europe. Geofluids 15, 464–482.

Sutskever, I., Martens, J., Dahl, G., Hinton, G., 2013. On the importance of initialization and momentum in deep learning. In: Proceedings of the 30th International Conference on Machine Learning. PMLR, Atlanta, Georgia, USA, pp. 1139–1147.

Tieleman, T., Hinton, G.E., 2012. Lecture 6.5-rmsprop: divide the gradient by a running average of its recent magnitude. COURSERA: Neural Netw. Mach. Learn. 4 (2), 26–31, 2012.

van der Walt, S., Colbert, S.C., Varoquaux, G., 2011. The NumPy array: a structure for efficient numerical computation. Comput. Sci. Eng. 13, 22–30.

van Rossum, G., 1995. Python Reference Manual. CWI. https://ir.cwi.nl/pub/5008.

Varsányi, I., Matray, J.-M., Ó Kovács, L., 1997. Geochemistry of formation waters in the Pannonian Basin (southeast Hungary). Chem. Geol. 140, 89–106.

Vaute, L., Aquilina, L., Gentier, S., Pinault, J.-L., Rose, P., 1998. Tests de traçage réalisés sur le site géothermique de Soultz-sous-Forêts (juillet-novembre 1997). Rapport d'essai. Rapport BRGM R 40320, 39.

Vidal, J., Genter, A., 2018. Overview of naturally permeable fractured reservoirs in the central and southern Upper Rhine Graben: insights from geothermal wells. Geothermics 74, 57–73.

Vidal, J., Hehn, R., Glaas, C., Genter, A., 2019. How can temperature logs help identify permeable fractures and define a conceptual model of fluid circulation? An example from deep geothermal wells in the upper rhine graben. Geofluids 2019, 1–14.

Wahba, G., 1987. Three topics in ill-posed problems. In: Inverse and Ill-Posed Problems. Elsevier, pp. 37–51.

Waskom, M., 2021. seaborn: statistical data visualization. JOSS 6, 3021.

Wood, C.P., 1992. Geology of the rotorua geothermal system. Geothermics 21, 25–41.

Yao, Y., Rosasco, L., Caponnetto, A., 2007. On early stopping in gradient descent learning. Constr. Approx. 26, 289–315.

Ystroem, L.H., Nitschke, F., Held, S., Kohl, T., 2020. A multicomponent geothermometer for high-temperature basalt settings. Geotherm Energy 8, 13.

Ystroem, L.H., Nitschke, F., Held, S., Kohl, T., 2021. An Integrated Sensitivity Analysis for the Basalt Specific Multicomponent Geothermometer for High Temperature Settings. World Geothermal Congress 2020+1. https://doi.org/10.5445/IR/1000104147.

Ystroem, L.H., Nitschke, F., Kohl, T., 2022. MulT_predict - an optimised comprehensive multicomponent geothermometer. Geothermics 105, 102548.